Porosity effect on ZrO$_2$ hollow shells and hydrothermal stability for catalytic steam reforming of methane†

Zi-Yian Lim,[ab] Chunzheng Wu,[a] Wei Guo Wang,[a] Kwang-Leong Choy[*c] and Hongfeng Yin[*a]

Hydrogen is an emerging energy source/carrier for oil refining and fuel cell applications. The development of an efficient and stable catalyst to produce hydrogen-rich gas is required for industrial application. The Ni@yolk-ZrO$_2$ catalyst could be a potential solution to tackle the challenges in hydrogen production. The catalyst was characterized using a combination of XRD, TEM, AAS, TPR, BET, and XPS. In this study, the amount of micropores in ZrO$_2$ hollow shells was demonstrated to influence the catalytic performance. Ni@yolk-ZrO$_2$ catalysts were evaluated for 48 hours under steam reforming of methane and their porosity effect in ZrO$_2$ hollow shells was identified. From the characterization of BET and catalytic evaluation, the physical information of the ZrO$_2$ hollow shell was established, which affected the catalytic performance in steam reforming of methane. Furthermore, the results from XPS and TEM showed that Ni particles were controlled under a ZrO$_2$ yolk−shell structure framework and showed the characteristic of moderately strong hydrothermal stability after the steam reforming test. The catalysts were studied at a GHSV of 50 400 mL g$_{cat}^{-1}$ h^{-1} and $S/C = 2.5$ at 750 °C and they remained stable with methane conversion more than 90% for 48 hours.

1. Introduction

In spite of the necessity to move towards renewable chemical resources in the future, the importance of large fossil fuels, especially natural gas based ones, will remain vital for a number of years. Therefore, the development of robust and efficient catalysts is a priority today. Steam reforming of methane (SRM) has attracted industrial interest because of the possibility to convert widely available carbon-based substances into feedstocks for further chemical processes.[1,2] Despite the drawbacks of the steam reforming of methane tied to its high endothermic reaction, this process produces hydrogen-rich synthetic gas. Since the SRM reaction runs at high temperatures, highly thermo-stable catalysts have to be developed for feed industry requirements. Ni-based catalysts have been considered to be a promising candidate due to their low cost and availability.[3] However, these catalysts suffered from fast deactivation at high temperatures due to sintering or particle growth and formation of inactive carbon fibres/filaments. These drawbacks become a main barrier for industrial applications.

Regarding the influence of the support on the activity of Ni-based catalysts, many studies have been reported. Doping with alkaline earth[4,5] and rare earth[6–8] elements or a substitute as the substrate[9–11] has been considered to be a promising strategy to promote nickel particle stability taking advantage of strong metal-support interactions. Other supports, in particular mesoporous structures,[12–14] were demonstrated to effectively disperse and confine active metal particles in mesoporous channels. Still, nickel particles' growth at high temperatures during pre-treatment and catalytic processes severely hurts the process of steam reforming of methane.[15,16] Therefore, the support should effectively promote uniform distribution of Ni particles and show thermal stability to support Ni particles.

The coking mechanism is well studied, as carbon severely deposited in the catalyst will eventually lead to deactivation because the sintering of active metal particles is dependent on the selection of supports. A study showed that highly dispersed Ni nano-clusters in MCM-41 have high stability in carbon dioxide reforming of methane at high temperatures.[17] The improved catalytic performance was suggested to be the result of high active centres on the pore wall surface and the stabilized dispersion of these active sites by the silica matrix. However, carbon deposition in a mesoporous channel support is inevitable. Many studies show that doping of other metals could

[a]Ningbo Institute of Material Technology and Engineering, 1219 Zhongguan West Road, Zhenhai District, Ningbo 315201, China. E-mail: yinhf@nimte.ac.cn

[b]University of Nottingham, Ningbo China, 199 Taikang East Road, University Park, Ningbo 315100, China. E-mail: zx08427@nottingham.edu.cn

[c]UCL Institute for Materials Discovery, University College London, Kathleen Lonsdale Building, Gower Place, London, WC1E6BT, UK. E-mail: k.choy@ucl.ac.uk; Tel: +44 (0) 207679 3855

suppress the growth of active metals in the mesoporous channel and lead to less carbon formation.[18–20]

Other approaches including the design of the support texture as core–shell or yolk–shell catalysts have also been reported recently.[21–26] These structures incorporate unique properties to prevent agglomeration of active metal nanoparticles. The structures were designed to encapsulate active metals with highly permeable shells to obtain reactant gaseous exchange and isolation of active metals simultaneously.[27] Many studies have demonstrated the effect of core–shell or yolk–shell structured supports[28–31] in catalyst applications. They each showed excellent stability and reusability for their respective catalytic process. Lately, Ni@porous silica-shells,[32] Ni@SiO$_2$ yolk–shell nanoreactors,[33] and Ni-yolk@Ni@SiO$_2$ nanocomposites[34] have been established in reforming of methane and outlined core–shell or yolk–shell structures were effective against active particle agglomeration at high temperatures. However, their Ni wt% loading was comparatively high for the reaction and among them Ni-yolk@Ni@SiO$_2$ nanocomposites have the suitable Ni loading. Also, the permeation degree of the respective shells was varied and influenced their yield of conversion of methane to syngas. SiO$_2$ as the shell support was shown to be effective in their respective reaction; however, the stability under water or water vapour is rather poor at high temperatures.[35,36] Motivated by these studies, we developed a catalyst with high stability for the steam reforming of methane reaction with a relatively low Ni loading while effectively isolating active Ni particles.

In this paper, we report a Ni@yolk-ZrO$_2$ catalyst synthesized *via* a double template emulsion method by varying the porosity of ZrO$_2$ hollow shells to investigate the catalytic performance and its stability in steam reforming of methane.

2. Experimental

2.1 Synthesis and characterization

Synthesis of Ni colloids and Ni@SiO$_2$. The synthesis of Ni@SiO$_2$ colloids was carried out by a reverse micelle approach. Typically, 3 mL of aqueous 0.25 M NiCl$_2$ and 11.5 mL of Brij L4 (Sigma-Aldrich) were mixed with 40 mL of *n*-octane in a 250 mL 3-neck round bottom flask at 30 °C under N$_2$ atmosphere protection. The mixture was stirred for 10 min before 1 mL of 3.172 M ice-cold NaBH$_4$ solution was quickly dropped into the flask. Immediately, a clear solution would turn pitch black and bubbles were generated. After 5 minutes of N$_2$ purge, the flask was sealed. Subsequently, the solution was stirred for 12 hours to form stable Ni colloids. The SiO$_2$ coating was achieved by subsequently adding 50 mL of *n*-octane, 2.4 mL Brij L4, 1.2 mL ammonia (26–28%), and 2 mL of TEOS into the solution and kept stirring for 3 hours. After 3 hours, additional 2 mL of TEOS was added and stirred for another 5 hours. The Ni@SiO$_2$ colloids were obtained after centrifugation and washed with acetone and ethanol, and then re-dispersed into 40 mL of ethanol.

Synthesis of Ni@SiO$_2$@ZrO$_2$. 35 mL of dispersed Ni@SiO$_2$ colloids in ethanol was used for the subsequent synthesis by mixing with 0.6 mL Brij L4, and 0.6 mL H$_2$O in 220 mL of ethanol and stirred for 30 minutes. Then, 2 mL of Zr(OBu)$_4$ was added and vigorously stirred for 8 hours at 30 °C. The colloids

were washed with ethanol twice and re-dispersed into 40 mL deionized water with 0.001 M NaBH$_4$ and aged for 3 days. The powder was collected and dried at 105 °C for 3 hours and calcined at 750 °C (2 °C min^{-1}) for 3 hours.

Synthesis of Ni@yolk-ZrO$_2$. The calcined powder was dispersed into 40 mL of 3 M NaOH solution and stirred for 48 hours. The colloids were washed with deionized water several times. After drying at 105 °C for 3 hours, the powder was calcined at 550 °C. Subsequently, the obtained powder was reduced under 10% H$_2$/Ar at 650 °C for 3 hours. During synthesis of Ni@SiO$_2$@ZrO$_2$, varying addition of Brij L4 from 0.0 mL, 0.4 mL, 0.6 mL, 0.8, and 1.2 mL will be denoted as BrNi-0.0, BrNi-1.6, BrNi-2.4, BrNi-3.2, and BrNi-4.8 respectively as the mole ratio of Brij L4-to-Ni.

Synthesis of Ni/ZrO$_2$. 1 g of commercially made ZrO$_2$ powder (TOSOH) was impregnated with 50 mL of 0.017 M NiCl and stirred at room temperature. After 6 hours, the obtained sol was dried at 100 °C for 3 hours and subsequently calcined at 750 °C for 3 hours, followed by reduction under 10% H$_2$/Ar at 650 °C for 3 hours.

X-ray diffraction patterns were recorded using a Bruker D8 Advance with Cu-Kα radiation ($\lambda = 1.5418$ Å) in the 2θ range of 10–90°. A transmission electron microscope (TEM), model JEM 2100, was used to study the morphology and microstructure of the catalyst. The TEM specimens were prepared by dropping a trace amount of the sample dispersed in ethanol on a carbon coated copper grid (300 mesh). The BET surface area measurement was carried out using a Micrometrics ASAP 2020M apparatus at 77 K. Prior to the measurement, the sample was degassed at 300 °C for 5 h under vacuum. Temperature-programmed reduction (FINE-SORB3010E, Zhejiang Fintec Co.) was performed to determine the nickel species and its reducibility for each catalyst. Typically, the catalyst was filled into a U-shape quartz tube and held by quartz wool. Prior to reduction, the sample was treated with pure Ar for 30 min at 300 °C to remove any impurities. The sample tube was then cooled down to room temperature. 10% H$_2$/Ar (25 mL min^{-1}) was introduced, and the temperature was increased from room temperature to 800 °C with a heating rate of 5 °C min^{-1}. X-ray photoelectron spectroscopy (XPS) spectra were recorded on a Shimadzu Axis Ultradld spectroscope (Japan) using a monochromatized Al Kα radiation source at room temperature and under a vacuum of 10^{-7} Pa (10^{-9} Torr). The starting angle of the photoelectron was set at 90°. The spectrum was calibrated with a C 1s spectrum of 248.8 eV.

2.2 Catalytic evaluation

Steam reforming of methane was studied in a fixed bed quartz reactor (12 mm ID) under atmospheric pressure. The reactor was equipped with a pre-heater, a syringe pump, a cold condenser and a gas flow meter. 100 mg of catalyst diluted with filled quartz sand of 2 cm length was used. The quartz reactor loaded with the catalyst was heated in an electric furnace and the temperature of the bed was controlled by using a K-type thermocouple positioned at the center of the catalyst bed. Prior to the test, the catalyst was reduced *in situ* 650 °C with 10% H$_2$/Ar mixture (50 mL min^{-1}) for 3 h. A reaction mixture of H$_2$O and CH$_4$ (steam to carbon molar ratio of 2.5 : 1) without dilution was fed using a gas hourly space velocity (GHSV) of 50 400 mL g$_{cat}^{-1}$ h^{-1}. The

effluent gases were analyzed by using an on-line gas chromato-graph (INESA Scientific Instrument Co. Ltd, GC-122) equipped with a packed column (TDX-01) and a TCD detector. A cold trap was placed before the TCD to remove moisture in the gas products. The peak area normalization method was used for quantitative analysis of effluent gases.[37,38] The CH$_4$ conversion and CO selectivity were calculated using eqn (1) and (2) as follows:

$$X_{CH_4}(\%) = \frac{[CO] + [CO_2]}{[CO] + [CO_2] + [CH_4]} \times 100 \qquad (1)$$

$$CO\ selectivity\ (\%) = \frac{[CO]}{[CO] + [CO_2]} \times 100 \qquad (2)$$

3. Results and discussion

XRD patterns of the catalyst are shown in Fig. 1a. The Ni@yolk-ZrO$_2$ catalyst shows the low crystallinity of Ni metal compared to the impregnated Ni/ZrO$_2$ catalyst. The catalysts showed the characteristic peaks of tetragonal ZrO$_2$ and Ni metal. The peaks observed at $2\theta = 44.5°$, $51.8°$, and $76.4°$ can be assigned to the (111), (200), and (220) planes of Ni metal, respectively. The average crystallite size of Ni was determined by the peak

(a)

(b)

Fig. 1 XRD patterns (a) and BET isotherm (b) of Ni@yolk-ZrO$_2$ and Ni/ZrO$_2$ catalysts.

broadening of the (111) reflection in the XRD patterns, using the Scherrer formula, and their respective crystallite size are shown in Table 1. The Scherrer equation was used to calculate the crystallite size which was compared with the particle size results obtained from the TEM study. This would help to give insight if increasing the surfactant concentration would affect the crystallite size. However, BrNi-4.8 has a relatively sharp peak of Ni at $2\theta = 44.5°$. ZrO$_2$ at $2\theta = 30.5°$ has the largest crystallite size among the catalysts excluding the reference sample Ni/ZrO$_2$. This indicates that excess addition of surfactant Brij L4 disfavours the dispersion of the Ni active metals in the ZrO$_2$ nano-framework. Also, the ZrO$_2$ grains in BrNi-4.8 were larger than other configurations.

The TEM micrographs of Ni@yolk-ZrO$_2$ catalysts before the steam reforming test are shown in Fig. 2. The Ni particles are uniformly distributed in the ZrO$_2$ hollow shell and no apparent aggregation of particles was observed. The particle distribution of Ni in each catalyst is shown in Table 1. It was observed that increased addition of the surfactant increased the Ni nano-particle size. The surfactant was employed as the porosity agent to achieve permeation of gaseous exchange for the ZrO$_2$ hollow shell. The increase in the Ni particle size with surfactant addition could be related to the total pore volume of the catalysts. Among the pore volumes, BrNi-4.8 has the lowest value of 0.18 cm^3 g^{-1}. Liu reported that for suppressing agglomeration of active metal nanoparticles, the substrates must possess two key properties: the uniformity of the active metal particles and abundance of micropores on the support.[39] The aspects of high uniformity of active metal nanoparticles were achieved, as observed by TEM. Subsequently, the catalysts (except BrNi-4.8) have moderately high total pore volumes of above 0.40 cm^3 g^{-1}, which indicates that the synthesized catalysts were able to suppress the agglomeration of the active metal nanoparticles. Also, the structural integrity of BrNi-4.8 collapsed after the steam reforming test (Fig. 3e), which implies that excessive addition of the surfactant in the Ni@yolk-ZrO$_2$ catalyst resulted in a fragile ZrO$_2$ hollow shell.

The BET isotherm graph (Fig. 1b) showed that the Ni@yolk-ZrO$_2$ catalyst has a Type-IV isotherm characteristic and a hysteresis loop of category H3 except in the case of BrNi-4.8, with a hysteresis loop of category H2. This shows that the addition of the surfactant leads to pore generation in the ZrO$_2$ hollow shell matrix. The TEM micrographs of all Ni@yolk-ZrO$_2$ catalysts have similar yolk–shell structures; however, the pore distributions were not similar. From Fig. 4, all the highest pore distributions of the catalysts were situated around 18 nm except BrNi-4.8, which presented the highest pore distribution situated at 4 nm. It was noted from TEM micrograph (Fig. S1†) that the void space of the Ni core and the ZrO$_2$ hollow shell was 19 nm. This indicated that excessive addition of the surfactant enlarged the pores existing in the ZrO$_2$ hollow shell and resulted in a channeled mesoporous characteristic in the BET isotherm graph. Besides, increasing addition of the surfactant Brij L4 leads to gradual interconnection of the pores of the ZrO$_2$ hollow shell, which affects the pore structure developed from the slit-shape to ink bottle, thus influencing the catalysts' efficiency. On the other hand, weak integrity of the ZrO$_2$ hollow shell could be ascribed to the hydrothermal
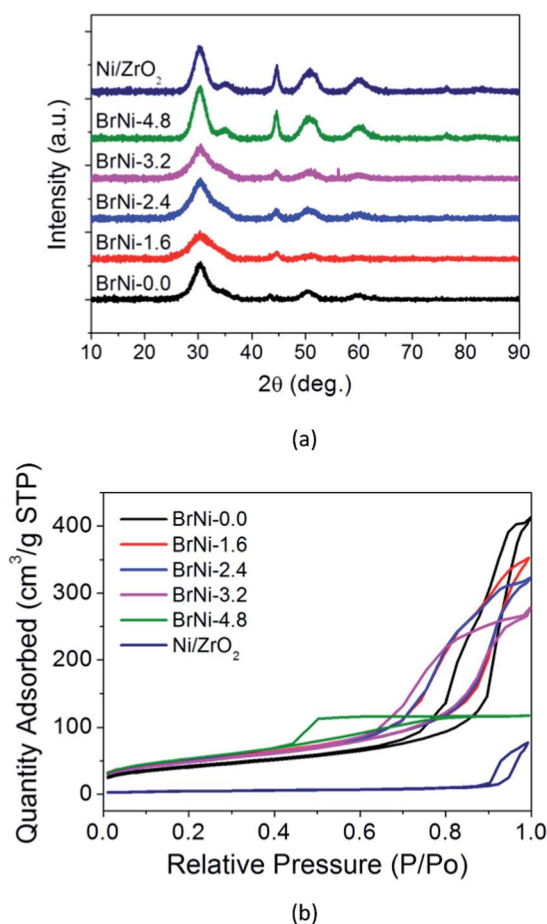
Table 1 Physical properties of Ni@yolk-ZrO$_2$ catalysts

Catalysts	Ni wt%	Crystallite size (nm)	Particle size (nm)	BET surface area (m^2 g^{-1})	Total pore volume (cm^3 g^{-1})	t-Plot micropore volume (cm^3 g^{-1})
BrNi-0.0	1.77	—	7.3	144.82	0.58	0.0037
BrNi-1.6	4.42	5.7	8.3	178.47	0.52	0.0087
BrNi-2.4	5.08	3.6	9.0	176.68	0.48	0.0095
BrNi-3.2	5.07	3.1	9.6	173.07	0.41	0.0039
BrNi-4.8	13.45	9.8	11.1	192.63	0.18	0.0019
Ni/ZrO$_2$	6.07	—	—	15.67	—	—
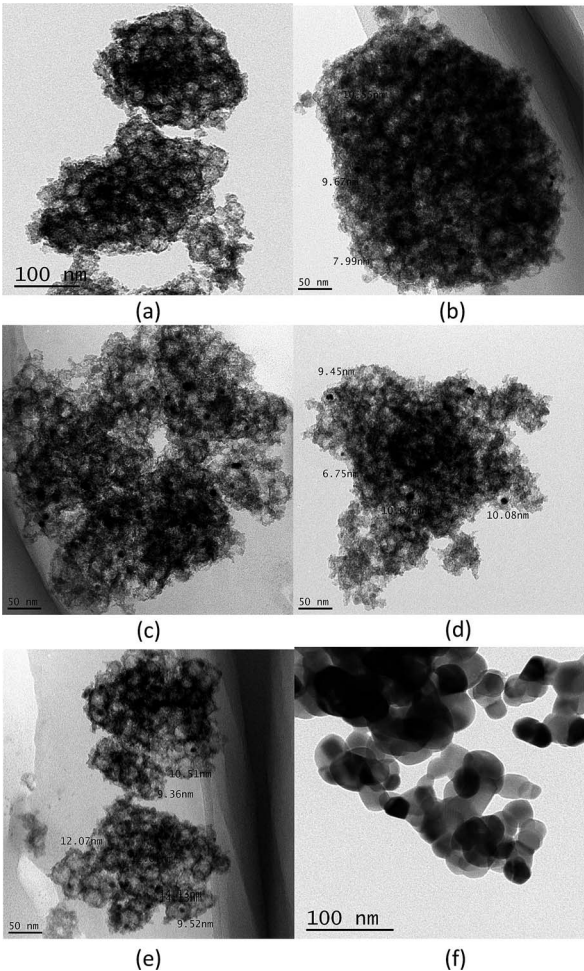
Fig. 2 TEM images of BrNi-0.0 (a), BrNi-1.6 (b), BrNi-2.4 (c), BrNi-3.2 (d), BrNi-4.8 (e), and Ni/ZrO$_2$ (f) before the steam reforming test.
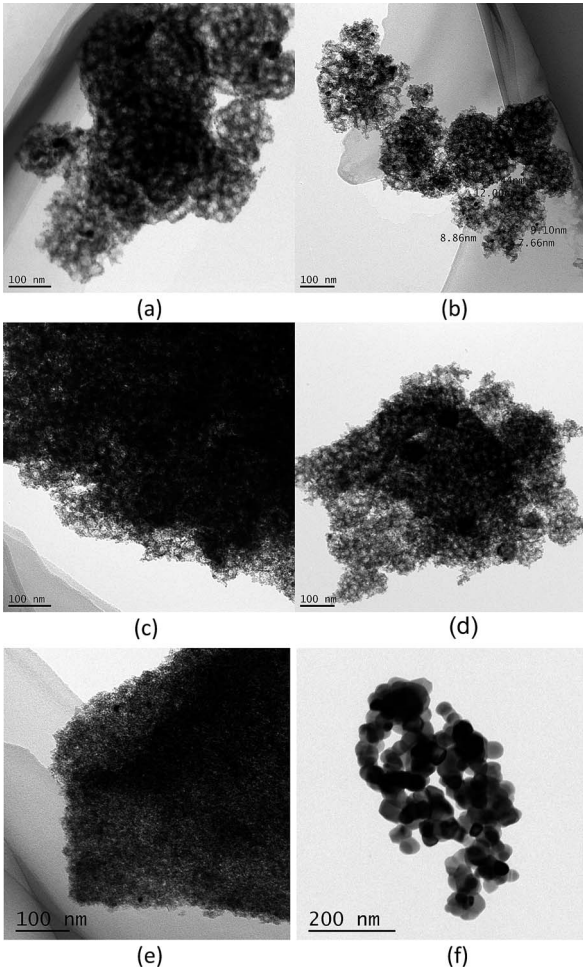
Fig. 3 TEM images of BrNi-0.0 (a), BrNi-1.6 (b), BrNi-2.4 (c), BrNi-3.2 (d), BrNi-4.8 (e), and Ni/ZrO$_2$ (f) after the steam reforming test.

instability of SiO$_2$ contributed in the shell matrix. From Table 2, BrNi-4.8 before and after the steam reforming test showed drastic changes in the Si 2p mass concentration over the catalyst surface when compared to other configurations. In addition, the O 1s XPS spectra from Fig. 5 of ZrO$_2$ (530 eV) and SiO$_2$ (532 eV) showed that, before testing, SiO$_2$ was detected at a lower intensity than ZrO$_2$, and higher intensity after the test. This implied that SiO$_2$ entities/matrix were disrupted in the shell and detected on the surface of the catalyst. It was proposed that SiO$_2$ was not a good selection as the support for steam reforming methane due to its hydrothermal instability at high temperatures.

Fig. 6 shows the Ni 2p XPS peak of Ni@yolk-ZrO$_2$ catalysts before and after the steam reforming test. Before the steam reforming test, Ni particles were detectable over the catalyst surface. In contrast, after testing, Ni particles were almost non-existent over the catalyst surface, with the exception of the configuration of the BrNi-4.8 catalyst. From XPS depth analysis, Ni particles have been detected partly in the matrix of the ZrO$_2$ hollow shell before testing and inside the hollow shell after steam reforming of methane testing. As for the BrNi-4.8 catalyst, it still displayed traces of Ni 2p mass concentration, while after steam reforming tests it was observed that Ni particles were not
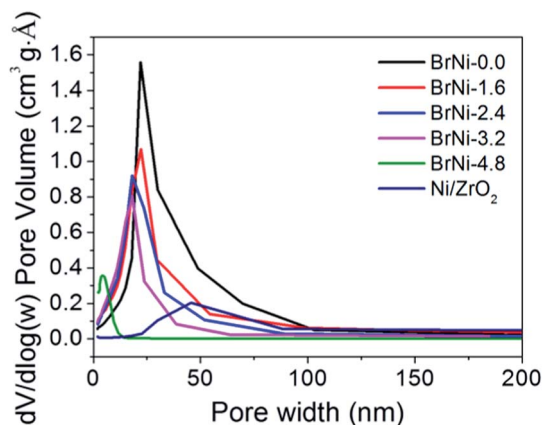
Fig. 4 Pore size distribution of the Ni@yolk-ZrO$_2$ catalyst and impregnated Ni/ZrO$_2$ catalyst.

Table 2 XPS analysis of the relative mass concentration of Ni@yolk-ZrO$_2$ and impregnated Ni/ZrO$_2$ catalysts before and after the steam reforming test

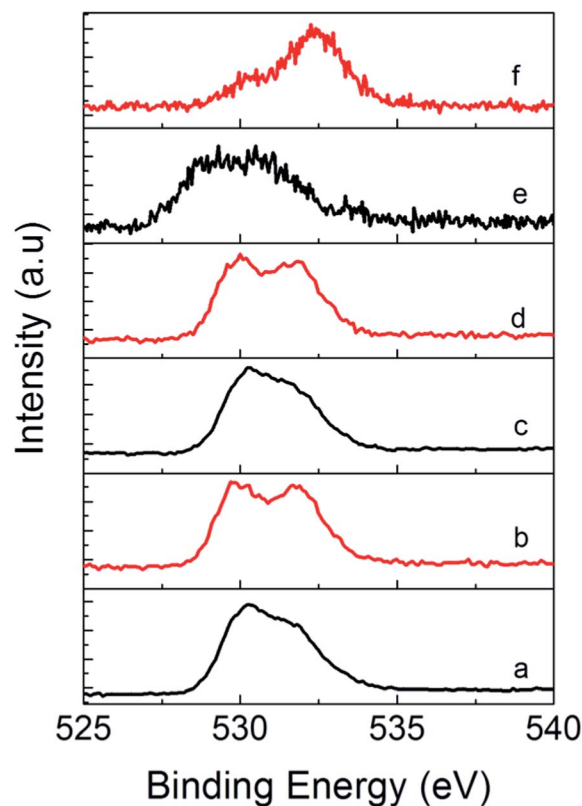| Catalysts	Ni 2p (%)	O 1s (%)	Zr 3d (%)	Si 2p (%)
BrNi-0.0-before	2.2	36.63	45.9	15.26
BrNi-0.0-after	0	34.95	43.21	21.83
BrNi-2.4-before	2.78	36.3	45.5	15.41
BrNi-2.4-after	0	31.13	40.02	22.69
BrNi-4.8-before	10.85	33.32	36.64	19.19
BrNi-4.8-after	2.67	40.68	25.12	31.53
Ni/ZrO$_2$-before	7.88	21.57	70.54	—
Ni/ZrO$_2$-after	7.49	36.13	56.38	—

Fig. 5 XPS O 1s spectra before (black line) and after (red line) the steam reforming test of BrNi-0.0 (a and b), BrNi-2.4 (c and d), and BrNi-4.8 (e and f) samples.

successfully encapsulated in the ZrO$_2$ hollow shell. Validation from the TEM micrograph in Fig. 3e showed that the structural framework of the BrNi-4.8 catalyst was collapsed after the steam reforming test. It is possible to conclude that excessive addition of the surfactant resulted in weak integrity of the ZrO$_2$ hollow shell which affected the stability of the catalyst during steam reforming of methane.

TPR analysis was carried out to evaluate the active Ni metal interaction with the ZrO$_2$ hollow shell support. As increasing addition of the surfactant resulted in a weaker ZrO$_2$ support, it lead to ease of mobility for Ni particles in the catalyst. Fig. 7 shows the patterns of reducibility of Ni in their configurations as of Ni@yolk-ZrO$_2$. BrNi-0.0 has highest 1$^{\text{st}}$ peak reduction temperature and gradually decreases to a lower reduction temperature as addition of the surfactant increased. The reducibility of the 2$^{\text{nd}}$ reduction peak gradually decreases to a lower reduction temperature, as strong metal-support interactions between Ni species and Zr species weaken due to the total pore volume decrease and the anchoring effect no longer sturdy to support the Ni particle. This indicated the amount of surfactant addition modifies the existing Ni species in the catalyst. From the BET isotherm graph, the onset of capillary condensation was shifting to a lower relative pressure, showing that the pores in the ZrO$_2$ hollow shell were enlarged as addition of the surfactant increased. It was evident from TPR testing that Ni species were affected by the pores of the ZrO$_2$ hollow shell.

3.1 Catalytic evaluation

The catalytic steam reforming of methane of Ni@yolk-ZrO$_2$ catalysts and impregnated catalysts as reference samples was studied at a GHSV of 50 400 mL g$_{\text{cat}}^{-1}$ h^{-1} and $S/C = 2.5$ at 750 °C, and the results are shown in Fig. 8. The methane conversion of Ni@yolk-ZrO$_2$ catalysts increased with time and the conversions were stable at 90% with time on stream, except BrNi-0.0 and BrNi-4.8. Initially, BrNi-0.0 showed high conversion of methane at 90% and dropped to 80% after 24 hours. The drop in conversion could be related to the low amount of micropores in the ZrO$_2$ hollow shell which does not support the gaseous exchange during the steam reforming test. As for BrNi-4.8, the low conversion was ascribed to the relatively large Ni particle size when compared with other configurations and the weak integrity framework of the ZrO$_2$ hollow shell.

Analysing the performances of the superior performance of these catalysts, the Ni particle size played an important role in the performance in steam reforming of methane. Comparing BrNi-2.4 with BrNi-4.8, the Ni particle size of 9 nm and 11.1 nm, respectively, greatly affected the methane dissociation during the steam reforming test. Another factor was the yolk–shell structure, which was stable after 48 hours of testing for BrNi-2.4, whereas the yolk–shell structure of BrNi-4.8 collapsed after 24 hours. The XPS Ni 2p and TEM images after the catalytic test showed the zirconia hollow shell effectively isolating the Ni particles with high structural stability, and maintaining high
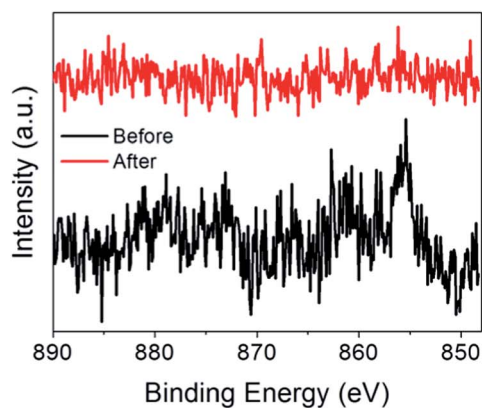
(a)
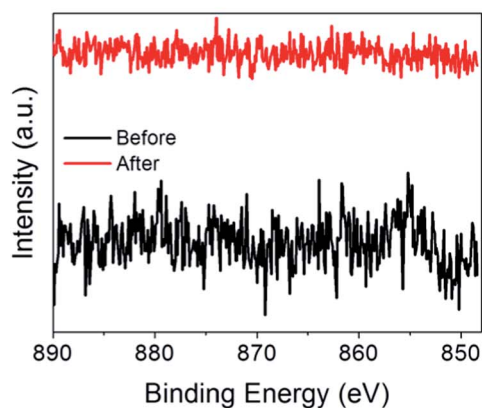
(b)
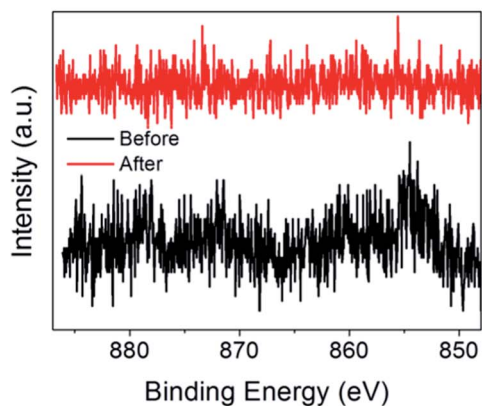
(c)

Fig. 6 XPS selected scan of the Ni 2p signal of BrNi-0.0 (a), BrNi-2.4 (b), and BrNi-4.8 (c) before and after the steam reforming test.
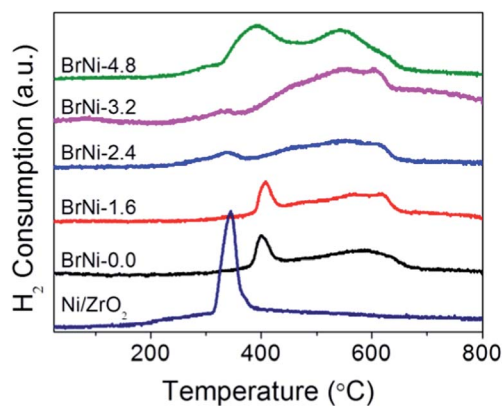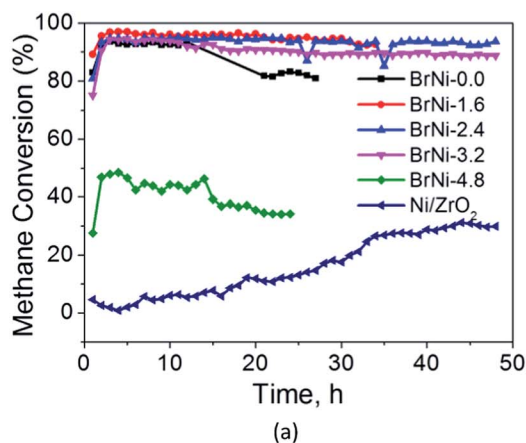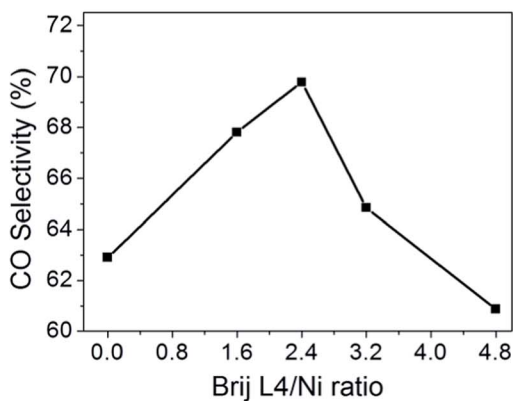

Fig. 7 Temperature-programmed reduction profile of Ni@yolk-ZrO$_2$ catalysts.

(a)

(b)

Fig. 8 Catalytic performance of steam reforming of methane on Ni@yolk-ZrO$_2$ and Ni/ZrO$_2$ catalysts (a). CO selectivity of Ni@yolk-ZrO$_2$ catalysts (b) at last point of reaction time.

performance in steam reforming of methane. The overall performance was low for BrNi-4.8 due to the weak integrity framework of the ZrO$_2$ hollow shell. XPS and TEM showed the entities of SiO$_2$ were greatly increased on the surface of the catalyst indicating the destruction of the ZrO$_2$ hollow shell. As for BrNi-0.0, the performance was slightly lower than that of BrNi-1.6, BrNi-2.4, and BrNi-3.2. The inhibition of the performance of BrNi-0.0 was ascribed to the physical characteristics of its ZrO$_2$ hollow shell. It showed a high amount of total pore volume but

has a low amount of micropore volume, indicating the low amount of slit-shaped pores in the ZrO$_2$ hollow shell, which was limiting the gaseous exchange in the steam reforming test. Also, the slit-shaped pores could be diminished due to sintering of ZrO$_2$ nano-grains in the ZrO$_2$ hollow shell, limiting the diffusion of reactants or products during steam reforming of methane.

4. Conclusions

Ni@yolk-ZrO$_2$ nanoparticles with sub-10 nm Ni cores were synthesized *via* a double template method and evaluated for steam reforming of methane. Active Ni particle agglomeration behaviour was studied by varying the pore size of the ZrO$_2$ hollow shell with surfactant addition. It was shown that the surfactant addition directly affected the physical properties of the ZrO$_2$ hollow shell and consequently its catalytic performance. Without surfactant addition, the ZrO$_2$ hollow shell limited the permeation of gases during the reaction, whereas, adequate addition of the surfactant promotes gaseous exchange. Over addition of the surfactant resulted in a weak ZrO$_2$ hollow shell. Besides, from XPS analysis, the hydrothermal stability of the catalysts was observed to be moderately strong in steam reforming of methane which favours long hours of the reaction. It is notable that the catalysts have both anti-agglomerating and good hydrothermal stability which is possible to extend to other similar reactions.

Notes and references

1 G. A. Olah, A. Goeppert, M. Czaun and G. K. S. Prakash, *J. Am. Chem. Soc.*, 2013, **135**, 648–650.

2 A. P. Simpson and A. E. Lutz, *Int. J. Hydrogen Energy*, 2007, **32**, 4811–4820.

3 G. Jones, J. G. Jakobsen, S. S. Shim, J. Kleis, M. P. Andersson, J. Rossmeisl, F. Abild-Pedersen, T. Bligaard, S. Helveg, B. Hinnemann, J. R. Rostrup-Nielsen, I. Chorkendorff, J. Sehested and J. K. Nørskov, *J. Catal.*, 2008, **259**, 147–160.

4 Z. Hou and T. Yashima, *Appl. Catal., A*, 2004, **261**, 205–209.

5 N. Sun, X. Wen, F. Wang, W. Wei and Y. Sun, *Energy Environ. Sci.*, 2010, **3**, 366–369.

6 L. Pino, A. Vita, F. Cipitì, M. Laganà and V. Recupero, *Appl. Catal., B*, 2011, **104**, 64–73.

7 V. R. Choudhary, K. C. Mondal and A. S. Mamman, *J. Catal.*, 2005, **233**, 36–40.

8 R. B. Duarte, O. V. Safonova, F. Krumeich, M. Makosch and J. A. van Bokhoven, *ACS Catal.*, 2013, **3**, 1956–1964.

9 N. Laosiripojana and S. Assabumrungrat, *Appl. Catal., B*, 2005, **60**, 107–116.

10 G. Jacobs, R. A. Keogh and B. H. Davis, *J. Catal.*, 2007, **245**, 326–337.

11 D.-W. Jeong, H.-S. Na, J.-O. Shim, W.-J. Jang, H.-S. Roh, U. H. Jung and W. L. Yoon, *Int. J. Hydrogen Energy*, 2014, **39**, 9135–9142.

12 H. Yin, Z. Ma, H. Zhu, M. Chi and S. Dai, *Appl. Catal., A*, 2010, **386**, 147–156.

13 Z.-J. Wang, Y. Xie and C.-J. Liu, *J. Phys. Chem. C*, 2008, **112**, 19818–19824.

14 S. Sokolov, E. V. Kondratenko, M.-M. Pohl, A. Barkschat and U. Rodemerck, *Appl. Catal., B*, 2012, **113–114**, 19–30.

15 J. Sehested, J. A. P. Gelten, I. N. Remediakis, H. Bengaard and J. K. Nørskov, *J. Catal.*, 2004, **223**, 432–443.

16 J. Sehested, *Catal. Today*, 2006, **111**, 103–110.

17 D. Liu, R. Lau, A. Borgna and Y. Yang, *Appl. Catal., A*, 2009, **358**, 110–118.

18 J. C. Guevara, J. A. Wang, L. F. Chen, M. A. Valenzuela, P. Salas, A. García-Ruiz, J. A. Toledo, M. A. Cortes-Jácome, C. Angeles-Chavez and O. Novaro, *Int. J. Hydrogen Energy*, 2010, **35**, 3509–3521.

19 S. Zhang, S. Muratsugu, N. Ishiguro and M. Tada, *ACS Catal.*, 2013, **3**, 1855–1864.

20 M. Lindo, A. J. Vizcaíno, J. A. Calles and A. Carrero, *Int. J. Hydrogen Energy*, 2010, **35**, 5895–5901.

21 J. Park and H. Song, *Nano Res.*, 2011, **4**, 33–49.

22 Y. Liu, Z. Fang, L. Kuai and B. Geng, *Nanoscale*, 2014, **6**, 9791–9797.

23 G. Li and Z. Tang, *Nanoscale*, 2014, **6**, 3995–4011.

24 V. Evangelista, B. Acosta, S. Miridonov, E. Smolentseva, S. Fuentes and A. Simakov, *Appl. Catal., B*, 2015, **166–167**, 518–528.

25 Q. Zhang, W. Wang, J. Goebl and Y. Yin, *Nano Today*, 2009, **4**, 494–507.

26 Q. Sun, X.-Q. Zhang, Y. Wang and A.-H. Lu, *Chin. J. Catal.*, 2015, **36**, 683–691.

27 J. Liu, S. Z. Qiao, J. S. Chen, X. W. Lou, X. Xing and G. Q. Lu, *Chem. Commun.*, 2011, **47**, 12578–12591.

28 H.-L. Jiang, T. Umegaki, T. Akita, X.-B. Zhang, M. Haruta and Q. Xu, *Chem.–Eur. J.*, 2010, **16**, 3132–3137.

29 S. H. Joo, J. Y. Park, C.-K. Tsung, Y. Yamada, P. Yang and G. A. Somorjai, *Nat. Mater.*, 2009, **8**, 126–131.

30 X. Huang, C. Guo, J. Zuo, N. Zheng and G. D. Stucky, *Small*, 2009, **5**, 361–365.

31 J. B. Joo, M. Dahl, N. Li, F. Zaera and Y. Yin, *Energy Environ. Sci.*, 2013, **6**, 2082–2092.

32 L. Li, S. He, Y. Song, J. Zhao, W. Ji and C.-T. Au, *J. Catal.*, 2012, **288**, 54–64.

33 J. C. Park, J. U. Bang, J. Lee, C. H. Ko and H. Song, *J. Mater. Chem.*, 2010, **20**, 1239–1246.

34 Z. Li, L. Mo, Y. Kathiraser and S. Kawi, *ACS Catal.*, 2014, **4**, 1526–1536.

35 H. Xiong, H. N. Pham and A. K. Datye, *Green Chem.*, 2014, **16**, 4627–4643.

36 M. Kanezashi and M. Asaeda, *J. Membr. Sci.*, 2006, **271**, 86–93.

37 Q. Wang, X. Li, W. Li and J. Feng, *Catal. Commun.*, 2014, **50**, 21–24.

38 X. Li, J. Feng, H. Fan, Q. Wang and W. Li, *Catal. Commun.*, 2015, **59**, 104–107.

39 Z. Liu, R. Che, A. A. Elzatahry and D. Zhao, *ACS Nano*, 2014, **8**, 10455–10460.